Rocket-based measurements of ion velocity, neutral wind, and electric field in the collisional transition region of the auroral ionosphere

L. Sangalli,[1] D. J. Knudsen,[1] M. F. Larsen,[2] T. Zhan,[2,3] R. F. Pfaff,[4] and D. Rowland[4]

[1] The JOULE-II sounding rocket salvo was launched from Poker Flat Rocket Range into weak pulsating aurora following a moderate substorm at 0345 LT on 19 January 2007. We present in situ measurements of ion flow velocity and electric and magnetic fields combined with neutral wind observations derived from ground observations of in situ chemical tracers. Measured ion drifts in the 150–198 km and 92–105 km altitude ranges are consistent with $\vec{E} \times \vec{B}$ motion to within 16 m s^{-1} rms and with neutral wind velocity to within 20 m s^{-1}, respectively. From these measurements we have calculated the ratio κ of the ion cyclotron and ion collision frequencies, finding $\kappa = 1$ at an altitude of 118 ± 0.3 km. Using direct measurements of ion current, we calculate the Joule heating rate and Pedersen and Hall conductivity profiles for this moderately active event and find height-integrated values of 390 W km^{-2} and 0.59 and 2.22 S, respectively. We also find that these values would have errors of up to tens of percent without coincident neutral wind measurements, and presumably more so during more active conditions. Ion flow vectors were measured at a rate of 125 s^{-1}; however, no significant fluctuations were observed at spatial/temporal scales below ~350 m and 0.5 s. Observational limits were 5.5 m and 0.016 s.

1. Introduction

[2] The lower ionosphere is a region in which ionospheric flows undergo a transition from magnetospheric to thermospheric control. Above ~150 km altitude, ions undergo $\vec{E} \times \vec{B}$ motion, whereas below ~100 km, they are fully entrained by the neutral wind. The transition between the two regimes is controlled by the ratio of ion cyclotron to ion collision frequencies, $\kappa_j = \Omega_j/\nu_j$, where j is a species index. Consequently, collision frequencies can be derived from independent measurements of electric and magnetic fields $\vec{E}$ and $\vec{B}$, bulk flow velocity $\vec{v}_j$, and neutral winds $\vec{U}$ [e.g., *Egeland et al.*, 1973].

[3] In situ measurements of $\vec{v}_j$ in the $\kappa_j \sim 1$ transition region are rare. The most common technique for measuring ion velocity $\vec{v}_i$ in the ionosphere, the ion drift meter/retarding potential analyzer [*Hanson et al.*, 1970; *Heelis et al.*, 1981] requires that ions be rammed into the instrument at high

Mach number, meaning at orbital speeds. But the collisional transition region is too low for orbiting satellites.

[4] There has been some success measuring E region ion drifts using electrostatic particle energy analyzers. A main challenge in this case is that the high voltages used in these detectors must be turned on in sufficiently low neutral pressures, typically above the E region. Moreover, the kinetic energies associated with ionospheric flows are quite small (in the milli-eV range) and can be influenced by changes in spacecraft potential and ion composition, small uncertainties in which can lead to significant measurement errors. Nevertheless, *Watanabe et al.* [1991] were able to measure bulk ion velocity in the 95–175 km altitude range using a curved-plate electrostatic analyzer as part the ERRRIS (E Region Rocket/Radar Instability Study) rocket campaign [*Pfaff et al.*, 1992]. Watanabe et al. found a significant deviation of ion velocity $\vec{v}_i$ from the $\vec{E} \times \vec{B}$ velocity below 125 km in quiet conditions, and below 160 km during a disturbed period. They also inferred that the ion collision frequency $\nu_i = \Omega_i$ at 115 km in the quiet case, however this estimate neglects the effects of neutral winds as they were not measured in that experiment.

[5] Incoherent scatter radar spectra are affected by ion collisions and can be used to derive collision frequency profiles [*Lathuillere et al.*, 1983; *Flå et al.*, 1985; *Huuskonen et al.*, 1986; *Nygren et al.*, 1987]. In practice this technique does not provide reliable results above about 100 km and

[1]Department of Physics and Astronomy, University of Calgary, Calgary, Alberta, Canada.
[2]Department of Physics and Astronomy, Clemson University, Clemson, South Carolina, USA.
[3]Currently at Conseco Inc., Carmel, Indiana, USA.
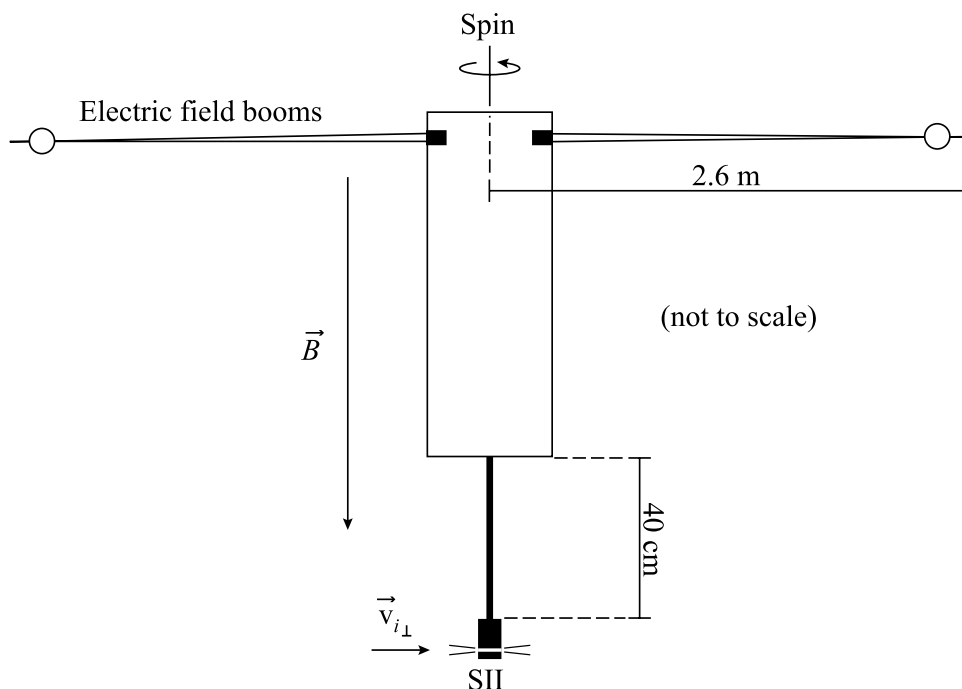[4]NASA Goddard Space Flight Center, Greenbelt, Maryland, USA.

Figure 1. The suprathermal ion imager (SII) is placed at the end of a boom aligned with the spin axis of the rocket. The field of view of the detector is 360° in the plane perpendicular to the magnetic field (with an out-of-plane angular acceptance of about ±3°), thereby allowing measurement of the ion drift velocity $\vec{v}_{i\perp}$ at high temporal and spatial resolution. In addition, four electric field booms, a magnetometer, and a Langmuir probe provided DC (0–1 kHz) electric field $\vec{E}_\perp$, magnetic field, and electron density measurements.

has poorer spatial and temporal resolution than is possible with in situ measurements. Nevertheless, ISR measurements can track the evolution and stability of measured parameters leading up to an in situ measurement and can be used as an independent check.

[6] In the present study we report recent (January 2007) measurements of ionosphere-thermosphere coupling parameters from the JOULE-II sounding rocket campaign. In addition to $\vec{E}$ and $\vec{B}$ measurements, JOULE-II carried a new generation of low-energy ion detector, the suprathermal ion imager (SII), and included chemical release rockets allowing neutral wind measurements in the altitude range 92–128.5 km.

[7] We proceed with an overview of the JOULE-II campaign and instrumentation in section 2, followed by a presentation of the measurements and derived quantities in section 3 and finally a discussion and conclusions in section 4.

2. Mission and Instrumentation

[8] JOULE-II, launched on 19 January 2007 from the Poker Flat Rocket Range (PFRR) in Alaska, consisted of two rockets carrying electric and magnetic field and particle instrumentation, two rockets releasing trimethyl aluminate (TMA) trails along the trajectories of the instrumented rockets, ground-based instruments consisting of three arrays of cameras used to track the TMA trails, coherent and incoherent scatter radars, magnetometers and two ground-based all-sky cameras at Poker Flat and Fort Yukon. One of the instrumented rockets, 21.138 University Experiments

(UE), carried instrumentation designed specifically to measure 2-D ion flow velocity in the plane perpendicular to the geomagnetic field $\vec{B}$ at a rate of $125\,\mathrm{s}^{-1}$, for direct comparison with the quantity $\vec{E} \times \vec{B}/B^2$. Figure 1 is a schematic of the payload showing its orientation relative to $\vec{B}$, the configuration of the electric field booms and the orientation and field of view of the low-energy ion detector (SII).

[9] The vehicle (21.138 UE) was launched at 1245 UT (0345 LT), reaching an apogee of 216.6 km and impacting ~293 km downrange after a flight time of 7.5 min.

[10] The geophysical conditions at the time of launch were characterized by moderate geomagnetic activity. Figure 2 shows an all-sky image taken from Fort Yukon and mapped onto a geomagnetic grid. The region to the south (bottom) is filled with faint, diffuse pulsating aurora with a thin, brighter northern boundary and little or no emission to the north. The trajectory of the 21.138 UE payload passed through the boundary at approximately 1250 UT and 197 km in altitude. Magnetometer deflections were approximately −400 nT at Poker Flat, and −200 nT at Fort Yukon (in H), respectively, ~148 km south and ~84 km east of the apogee.

2.1. Suprathermal Ion Imager

[11] The SII sensor head is a 3.7-cm-diameter, 12-cm-long cylinder mounted with its axis parallel to the payload spin axis and displaced afward of the bottom deckplate by a 40-cm-long boom, as depicted in Figure 1. The external skin of the sensor was held at −2 V with respect to the payload floating potential in order to draw in low-energy positive ions. Inside the sensor, the SII uses two concentric hemispherical grids to form 2-D (angle/energy) maps of low-
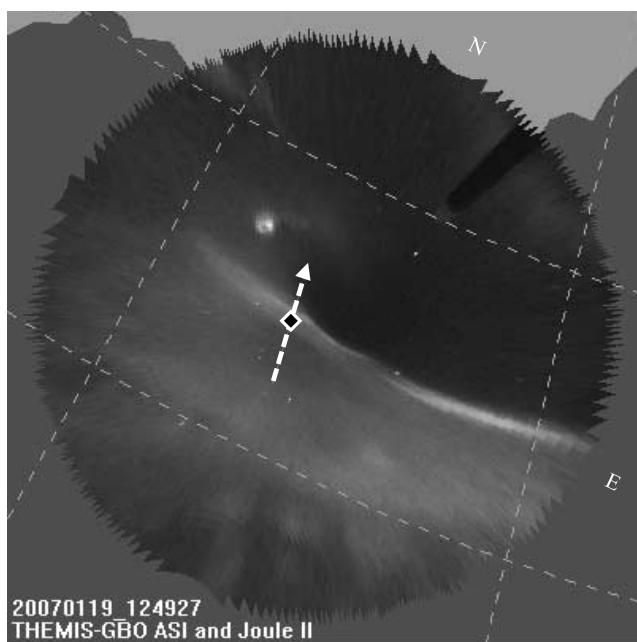
Figure 2. All-sky camera image taken from Fort Yukon. The thick dashed line is the trajectory of the payload 21.138 UE as it moves northward (upward in the plot). The diamond shows its position at 1249:27 UT, ∼300 s after launch. (Geomagnetic coordinate projection of camera and trajectory data courtesy of E. F. Donovan.)

energy ($0-10$ eV) ion distribution functions (see Figure 3). In the orientation shown in Figure 1, the SII samples continuously in the plane perpendicular to $\vec{B}$.

[12] The SII differs from the more common "top hat" analyzer [*Carlson et al.*, 1982] in that its focusing system images the energy distribution (rather than stepping through energy with time), and is optimized for lower-energy particles [*Whalen et al.*, 1994; *Knudsen et al.*, 2003]. The resulting particle flux distribution is amplified using a microchannel plate and phosphor screen, then reduced in diameter 3:1 and transferred through a 1-m-long coherent fiber-optic imaging bundle. Images are recorded in the SII power and control unit by a 256×256-pixel charge-coupled device (CCD). For JOULE-II, pixels are binned 4×4 on chip, sampled with an 8-bit A/D converter, and binned again 2×2 in software to produce 32×32-pixel images at a rate of 125 s^{-1}. The position and size of the ion images are related to bulk ion velocity and temperature, respectively. This paper is concerned with the velocity measurements.

[13] The JOULE-II SII CCD was not cooled actively and operated at a temperature between $+20°$ and $+30°$C. The 8-bit sampling is consistent with the dynamic range of the CCD, which in turn is determined primarily by the operating temperature, on-chip binning scheme and frame rate.

2.2. Electric Field Instrument

[14] For the JOULE-II experiment, the DC and AC vector electric fields were measured along the rocket trajectory using the standard double probe technique (see review by *Pfaff* [1996]). In this case, spherical sensors with embedded

preamps were extended on fiberglass booms in the spin plane with separation distances of 5.2 m tip-to-tip for two orthogonal double probes. Since the payload spin axis was oriented along the magnetic field direction to within a few degrees, the two-dimensional double probe measurement completely parameterized the DC electric field solution, since we assume no parallel electric field existed in the low-altitude auroral ionosphere. The DC electric field data were gathered with a time resolution of 1 m s^{-1} and sampled with 18-bit A/D converters on board the rocket payload. After the data were telemetered to the ground, offsets were easily identified and removed from the data which displayed clear sine waves at the payload spin frequency. The $\vec{V}_{payload} \times \vec{B}$ fields were then subtracted and the resulting DC electric field components were rotated from the payload coordinates to geomagnetic coordinates using the gyroscope attitude solution. The accuracy of the measurement depends on several factors and is generally ±0.5 mV/m corresponding to approximately 10 m s^{-1}.
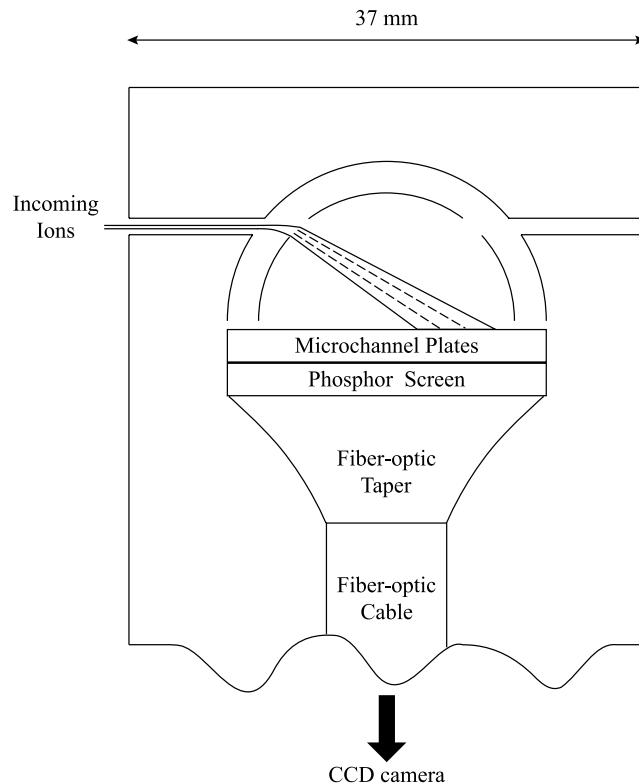

Figure 3. The schematic of the SII is a cross section of the cylindrical sensor. Ions enter the detector through the aperture, pass through a region of static electric field between the two hemispherical electrodes, and traverse a field-free region within the inner electrode to create a 2-D energy/angle ion spectrogram. Ions at the upper end of the energy range land by the inner electrode while the least energetic land close to the center. The microchannel plates, the phosphor screen, the fiber-optic taper and cable, and the charge-coupled device constitute the imaging system. The exterior skin of the SII is maintained at a potential of -2 V relative to the payload potential.
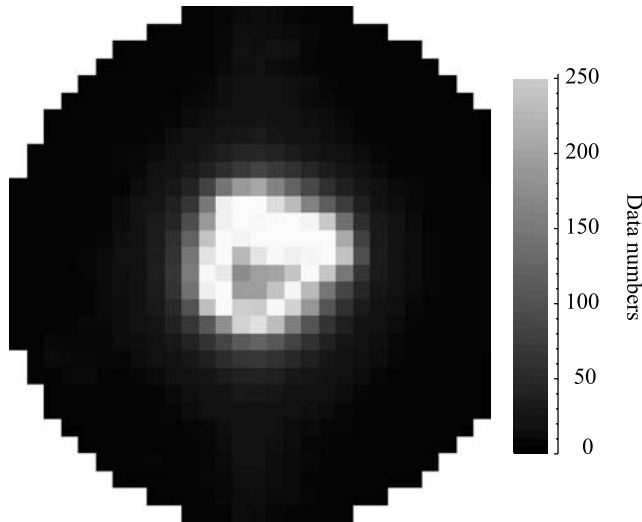
Figure 4. Example of an SII image 290 s after launch. Gray scale indicates the number of counts for each pixel, with white being the highest and black the lowest. Each image consists of 729 pixels, and the sampling rate is 125 frames per second. The slight brightening in the top part of the image is due to the effects of ram velocity. Ion velocity is determined from the 2-D centroid of each SII image.

2.3. Chemical Release Experiment

[15] Each instrumented payload in the experiment was paired with a chemical release payload launched one minute later to provide neutral wind profile measurements in the lower E region. The data analysis in this paper focuses on the measurements obtained from the flight of 41.065 UE, which was launched at 1246 LT. The rocket released upleg and downleg trimethyl aluminum (TMA) trails that produce a visible chemiluminescent tracer of the neutral flow that can be tracked with ground-based cameras over periods of 5–10 min or longer. The camera sites used in the experiment were all in Alaska and included Poker Flat, Fort Yukon and Coldfoot. The Coldfoot site had too much cloud cover at the time of launch to be useful but the triangulation to determine the movement of the trails as a function of height and thus the wind profiles was carried out successfully with the two available sites. The trails that were deployed yielded useful wind results in the height range between approximately 90 and 140 km altitude on the upleg and approximately 90 and 130 km altitude on the downleg. The uncertainties in the wind determination are in the range from 5–10 m s^{-1}. The upleg and the downleg profiles showed similar features and wind speeds in the altitude range where they overlapped, suggesting that the latitudinal gradients were relatively small at this time in the event.

3. Measurements

3.1. In-Flight Calibration of Ion Velocity

[16] Figure 4 is a raw SII image taken 290 s after launch, at an altitude of 202 km during the downleg of the flight. The slight asymmetry to one side is due to the ram effect; this feature orbits the center of the image at the payload spin period of 1.54 s. The −2V sensor bias added to the payload-to-plasma potential imparts a minimum energy to all in-

coming ions and is responsible for the circular region of lower signal near the image center. To extract the ion drift velocity from each image, we calculated the position of its centroid $\vec{r}$:

$$\vec{r} = \frac{\sum_{x,y} C_{xy}(x\hat{x} + y\hat{y})}{\sum_{x,y} C_{xy}} \quad (1)$$

where C_{xy} is the pixel count at pixel position (x, y).

[17] In Figure 5 (top) we compare the image centroid positions along x and y with the corresponding $\vec{E} \times \vec{B}$ velocity components just after apogee (for 10 payload spins). These plots also show linear fits and fit coefficients. In order to obtain final calibration coefficients we averaged fit parameters taken over two intervals: 206–198 km (shown in Figure 5) and also 166–150 km, both of which occurred during the descent, placing the SII sensor in the ram direction and free from wake disturbances. These intervals were chosen to be at altitudes where it can be assumed that $\vec{v}_i = \vec{E} \times \vec{B}/B^2$ to a good approximation. Two separate intervals were chosen to try to account for large-scale trends in parameters that could affect the calibration, such as average ion mass or spacecraft potential. This choice was justified after the fact by a 30% reduction in errors determined by comparing ion velocity with $\vec{E} \times \vec{B}$ in the range 166–198 km, and with neutral winds in the range 92–105 km. We note that the payload was aligned to the geomagnetic field to within 3° throughout both calibration intervals, meaning errors resulting from payload misalignment with $\vec{B}$ were negligible. An example of the resulting ion drift velocity and $\vec{E} \times \vec{B}$ components is presented in Figure 5 (bottom).

[18] We note that the above calibration is strictly empirical in that it exploits an observed linear trend between ion velocity and measured $\vec{E} \times \vec{B}$. Even so, it is consistent with instrument Monte-Carlo simulations [Burchill, 2003] showing that total ram velocity is related to radial centroid as follows:

$$E_{tot} = \frac{m_i}{2}v_r^2 - q_i\Phi_{s/p} = a\left(\frac{r}{R}\right)^p \quad (2)$$

where E_{tot} is the kinetic energy of rammed ions after traversing the sensor-to-plasma potential difference $\Phi_{s/p}$, m_i and q_i are the ion mass and charge, v_r is the ram speed, r is the radial distance of the centroid relative to the detector center, R is the inner diameter of the inner hemispherical electrode (see Figure 3) and a and p are fit parameters. Simulations show $p \approx 1.8$, which for small $\Phi_{s/p}$ implies $v_r \propto r^{0.9}$.

[19] To determine the ion velocity we use the observed linear relationship instead of equation (2) because ion composition and sensor-to-plasma potential are not measured. Even small uncertainties in these parameters lead to large errors in ion velocity. However, as we show in section 3.2, such errors were not important in the case of JOULE-II.

3.2. Velocities

[20] The ion velocity resulting from the operations described above is in payload coordinates. Using the gyroscope-based payload attitude solution, we transformed to local geographic coordinates. Each component was then smoothed with a boxcar filter of length equal to the spin period in order to remove residual errors in the transformation
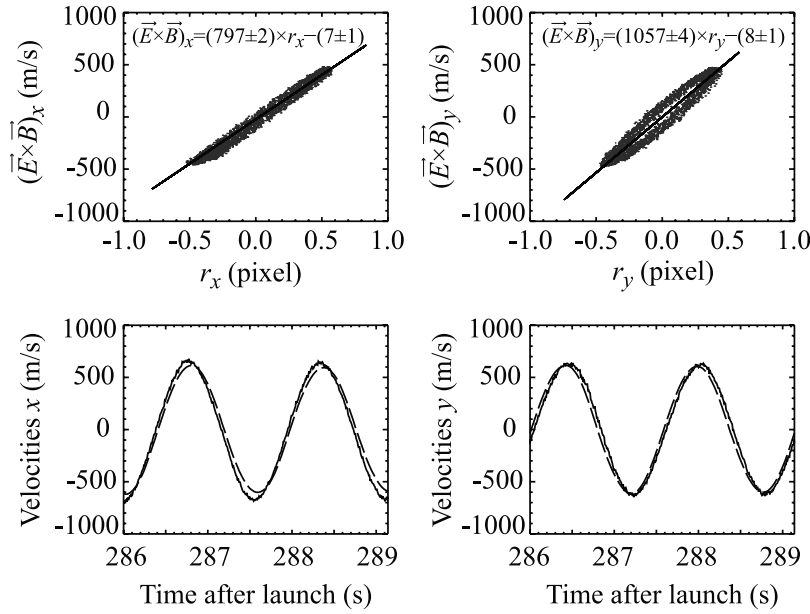
Figure 5. Calibration of the ion drift velocity against the $\vec{E} \times \vec{B}$ drift velocity. We calculate the centroid position (r_x, r_y) of each SII image in rocket-based coordinates. Then, we use a linear fit to relate the ion centroid positions to the $\vec{E} \times \vec{B}$ velocity, shown in the top. The resulting ion velocity (solid black line) is shown in the bottom along with $\vec{E} \times \vec{B}$ (dashed line) for two cycles within the calibration interval 281–297 s after launch.

at the spin frequency and its harmonics. We then use an International Geomagnetic Reference Field (IGRF)-based conversion to local geomagnetic coordinates (east, north and antifield aligned [E,N,U]). The smoothed downleg ion velocity components of $\vec{v}_i$ are shown in solid black in Figure 6, along with $\vec{E} \times \vec{B}$ velocity components (dotted line) and the TMA-derived neutral wind velocity components $\vec{U}$ (dashed line). Above 150 km, the root-mean-square difference between the ion and $\vec{E} \times \vec{B}$ velocity components is 13 m s^{-1} eastward and 15 m s^{-1} northward, quantifying the accuracy to which SII-derived velocity components track $\vec{E} \times \vec{B}$ outside of the calibration interval (above 166 km and below 198 km).

[21] Below 140 km, the ion flows begin to depart significantly from the $\vec{E} \times \vec{B}$ drift velocity. This behavior of the ions is expected in the lower ionosphere where they become affected by collisions with the neutrals. Still, it is worth considering possible sources of error that could cause ion drifts to be different from the $\vec{E} \times \vec{B}$ velocity. For example equation (2) shows that the ion velocity measurement depends on the payload floating potential through the sensor-to-plasma potential $\Phi_{s/p}$ as well as the ion mass, neither of which were measured in this study. Changes in these parameters introduce potential sources of error and could cause a deviation of $\vec{v}_i$ from $\vec{E} \times \vec{B}$ as seen below 140 km. Yet, below about 110 km $\vec{v}_i$ approaches the neutral wind velocity $\vec{U}$ such that in the altitude range 92–105 km the two velocity components agree to within 20 m s^{-1} in the east and 17 m s^{-1} in the north directions (rms difference). This constitutes an independent validation of the ion velocity, indicating that the deviation of $\vec{v}_i$ from $\vec{E} \times \vec{B}$ is not due to a measurement artifact such as a change in payload potential or ion composition.

[22] Ion demagnetization is even more evident in Figure 7 (left), where we show the ratio of ion speed to $\vec{E} \times \vec{B}$ speed

(solid line) and the ratio of ion speed to neutral wind speed (dashed line). The ratio of ion speed to $\vec{E} \times \vec{B}$ speed and to neutral wind speed is close to unity for altitudes above 140 km and below 105 km, respectively. In Figure 7 (right) we show the deviation from the electric field direction for the ions (solid line) and the neutral wind (dashed line). Below 130 km the angle between ion velocity and electric field decreases from 90° to almost zero at which point the ions become highly demagnetized and their direction of travel turns to match that of the neutral wind.

3.3. Collision Frequency

[23] We now use the velocity measurements described in section 3.2 to derive κ, the ratio of the ion cyclotron frequency (Ω_i) to the ion collision frequency (ν_i) from the equation of motion:

$$nm_i \frac{\partial \vec{v}_i}{\partial t} = q_i n (\vec{E} + \vec{v}_i \times \vec{B}) - nm_i \nu_i (\vec{v}_i - \vec{U}) \tag{3}$$

where n is the plasma density. Under the guiding center approximation, using $\Omega_i = |qB|/m_i$ and assuming steady state conditions such that we can neglect $\frac{\partial}{\partial t} \ll \Omega_i$

$$0 = \Omega_i \left(\frac{\vec{E}}{B} + \frac{\vec{v}_i \times \vec{B}}{B} \right) - \nu_i (\vec{v}_i - \vec{U}) \tag{4}$$

yielding

$$\Omega_i \left| \frac{\vec{E}}{B} + \frac{\vec{v}_i \times \vec{B}}{B} \right| = \nu_i |\vec{v}_i - \vec{U}| \tag{5}$$
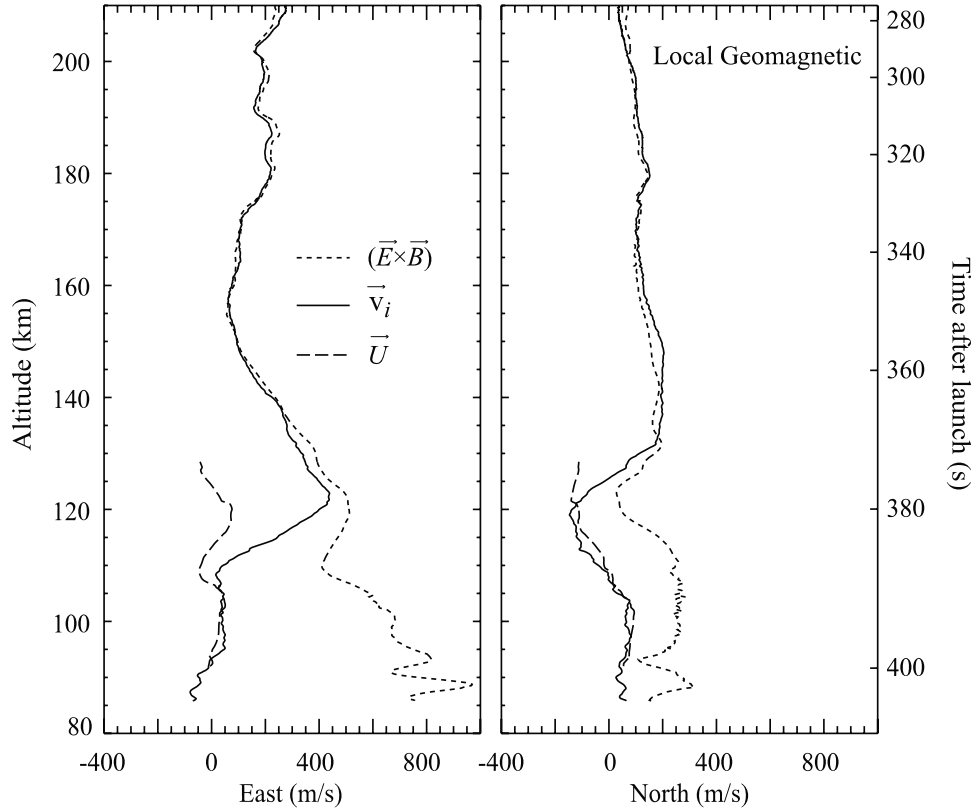
Figure 6. Comparison between ion drift velocity components $\vec{v}_i$ (solid black line), $\vec{E} \times \vec{B}$ drift velocity components (dotted line) and the neutral wind velocity components $\vec{U}$ (dashed line) in the local geomagnetic frame for the flight downleg. The ion velocity $\vec{v}_i$ is calibrated against $\vec{E} \times \vec{B}$ during the descent using an average of the altitude ranges 198–206 km and 166–150 km. The neutral wind velocity $\vec{U}$ is obtained from trimethyl aluminate trails.

thus,

$$\kappa = \frac{\Omega_i}{\nu_i} = \frac{|\vec{v}_i - \vec{U}|}{\left| \frac{\vec{E}}{B} + \frac{\vec{v}_i \times \vec{B}}{B} \right|} \qquad (6)$$

The resulting altitude profile for κ is shown in Figure 8 in solid black from which we see that the altitude where $\kappa = 1$ is 118 km. For uncorrelated errors, the error on the value of κ is the following:

$$(\Delta\kappa)^2 = \left(\frac{\Delta|\vec{v}_i - \vec{U}|}{\left| \frac{\vec{E}}{B} + \frac{\vec{v}_i \times \vec{B}}{B} \right|} \right)^2 + \left(\frac{|\vec{v}_i - \vec{U}|}{\left| \frac{\vec{E}}{B} + \frac{\vec{v}_i \times \vec{B}}{B} \right|^2} \Delta \left| \frac{\vec{E}}{B} + \frac{\vec{v}_i \times \vec{B}}{B} \right| \right)^2 \qquad (7)$$

using the rms speed differences for $\Delta|\frac{\vec{E}}{B} + \frac{\vec{v}_i \times \vec{B}}{B}|$ and $\Delta|\vec{v}_i - \vec{U}| - 10$ m s^{-1} and 14 m s^{-1}, respectively. The error on the altitude for which $\kappa = 1$ is 0.3 km. Below 105 km, the estimate of κ is unreliable since errors become comparable to κ itself. To quantify the improvement realized from the neutral wind measurements, we have recalculated the ion collision frequency profile assuming $\vec{U} = 0$, shown by the dotted line in Figure 8. These data give a value of $\kappa = 1$ at ~116.5 km, meaning an altitude error of 1.5 km.

3.4. Joule Heating and Conductivities

[24] Joule heating $\vec{J} \times \vec{E}$ is the rate of electrical to mechanical energy conversion. *Vasyliūnas and Song* [2005] point out that this calculation should be carried out in the frame of the plasma, which is defined predominantly by the ions. More commonly, it is calculated in the reference frame of the neutral atmosphere, in which case it is interpreted as the sum of plasma heating, heating of the neutral gas, and work done on the plasma. We calculate the latter quantity $\vec{J} \times \vec{E}'$, where the electric field seen in the neutral frame is $\vec{E}' = \vec{E} + \vec{U} \times \vec{B}$:

$$\vec{J} \cdot \vec{E}' = nq_i(\vec{v}_i - \vec{v}_e) \cdot \vec{E}' \qquad (8)$$

For the altitudes of interest in this study, electrons remain magnetized and v_e can be replaced by the $\vec{E} \times \vec{B}$ velocity. Figure 9 shows the resulting Joule heating profile, which peaks at an altitude of 114 km and has a height-integrated value from 110 to 128.5 km of 0.38 kW per square kilometer. To illustrate the importance of neutral winds in this calculation, Figure 9 also shows the Joule heating profile for which neutral wind velocities are neglected. This gives a height integrated value that is 28% too large.
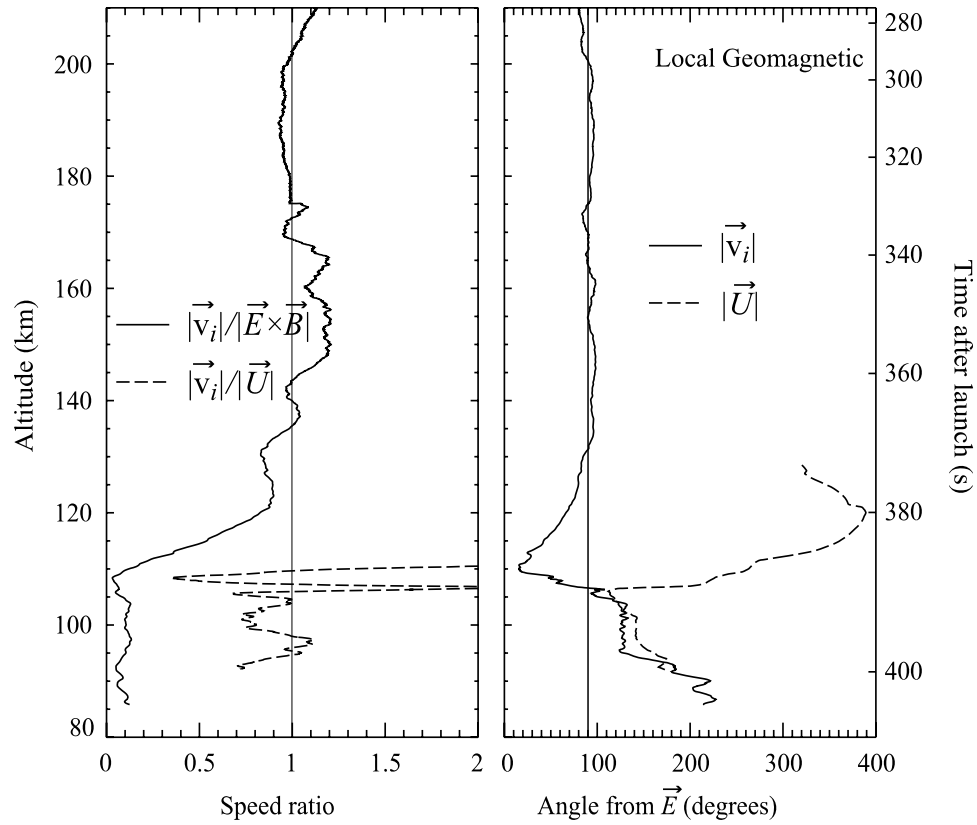
Figure 7. (left) Ratio of ion speed $|\vec{v}_i|$ to $|\vec{E} \times \vec{B}|$ speed (solid line) and the ratio of $|\vec{v}_i|$ to neutral wind speed $|\vec{U}|$ (dashed line) in the local geomagnetic frame for the flight downleg. (right) Angle between the ion velocity $\vec{v}_i$ and the electric field (solid line) and the neutral wind velocity $\vec{U}$ and the electric field (dashed line). Positive angle is measured counterclockwise as viewed looking downward along $\vec{B}$.
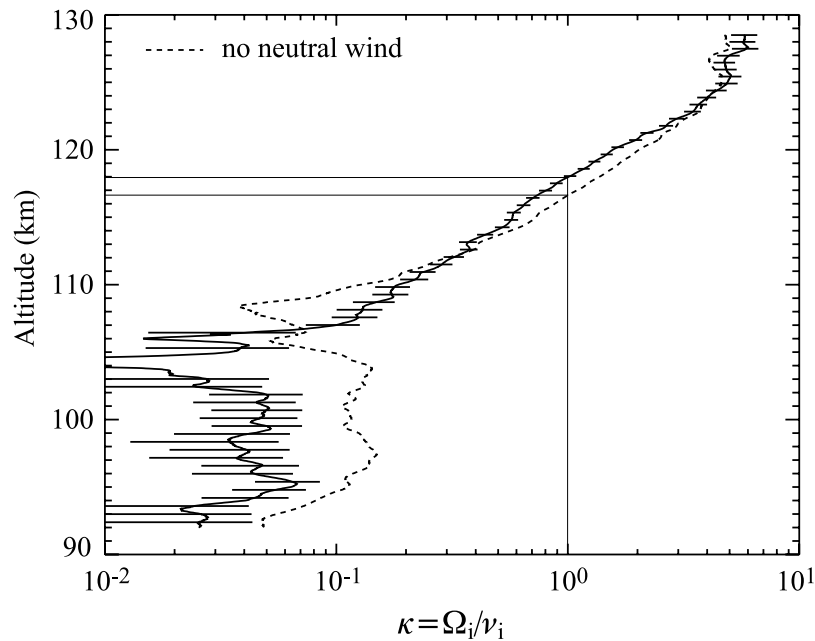
Figure 8. The ratio κ of ion cyclotron frequency Ω_i to ion collision frequency ν_i (derived using equation (6)) is shown as a solid black line using the measured neutral wind velocity and as a dotted line for $\vec{U} = 0$. The error bars are plotted every 50 points and their values obtained from equation (7). Data below 107 km indicate the measurement resolution and are nonphysical.
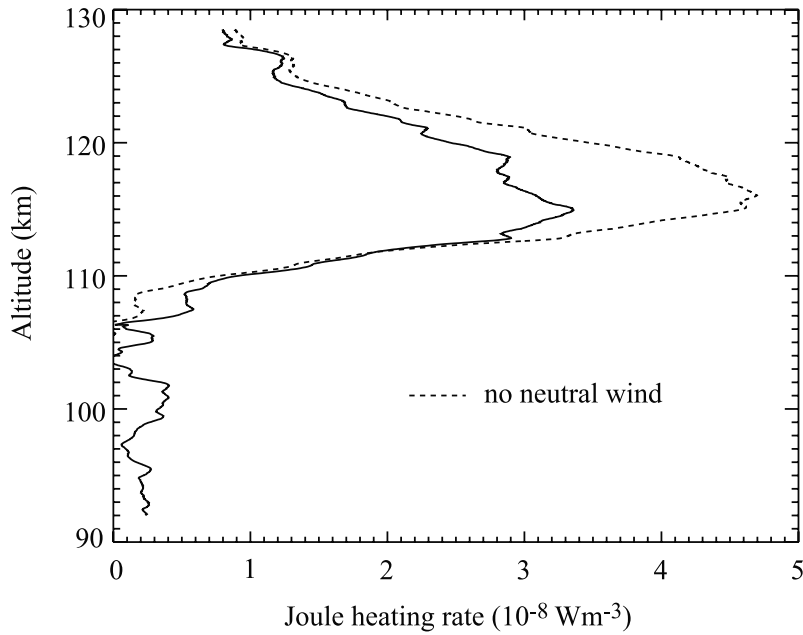
Figure 9. Joule heating rate profiles taking into account the neutral wind (solid line) and neglecting the neutral wind (dashed line). Note that this is not a true vertical profile owing to the northward motion of the rocket.

[25] Using this knowledge of the Joule heating profile, we can also estimate the Pedersen and Hall conductivities as follows:

$$|\vec{J}_P| = \vec{J} \cdot \frac{\vec{E}'}{|\vec{E}'|} = \sigma_P |\vec{E}'| \qquad (9)$$

$$|\vec{J}_H| = \vec{J} \cdot \frac{\vec{E}' \times \vec{B}}{|\vec{E}' \times \vec{B}|} = \sigma_H |\vec{E}'| \qquad (10)$$

Figure 10 shows the Pedersen and Hall conductivity profiles calculated from equations (8)–(10) along with the electron density derived from the Langmuir probe to show its contribution to structure in the conductivities. Height-integrated values are given in Table 1. The error in Σ_P and Σ_H resulting from neglecting the neutral wind is +14% and −6%, respectively.

[26] Table 1 also includes an estimate of the height-integrated Joule dissipation calculated from direct integration of $\vec{J} \cdot \vec{E}$.

4. Discussion and Conclusions

[27] In the altitude range 105–115 km, the ion velocity does not lie between the $\vec{E} \times \vec{B}$ velocity and neutral wind velocity, which is unphysical and presumably indicates a measurement error. Below we consider two potential error sources: spacecraft charging, which could induce an ion velocity error, and a change in convection flow in the several minute period between the ion and neutral wind measurements; we will show that the latter is the more likely explanation.

4.1. Ion Velocity Errors

[28] Figure 6 shows that above 150 km altitude, eastward ion drifts agree with $\vec{E} \times \vec{B}$ motion to within 15 m s^{-1} rms. Ions become increasingly entrained in the neutral wind below that altitude, and they follow the neutral wind below 105 km, to within 20 m s^{-1} rms. In the northward direction, ions also follow $\vec{E} \times \vec{B}$ motion at high altitudes (to within 16 m s^{-1} rms) and neutral winds below 105 km (to within 17 m s^{-1} rms). In the altitude range 105–115 km, the ion velocity does not lie between the $\vec{E} \times \vec{B}$ velocity and the neutral wind velocity which is unphysical and presumably indicates a measurement error. There is a possibility that the northward ion velocity measurement is perturbed owing to a change in spacecraft potential in this region. Arguing against this is the apparent absence of any large error in the eastward component. However, a spacecraft potential change affects the ram component of ion flow most strongly, which is nominally northward for JOULE-II. To estimate the sensitivity of the ion velocity to the spacecraft potential we take the derivative of equation (2). A transient change in spacecraft potential could induce an error $\Delta v_r = q_i \Delta \Phi / (m_i v_r)$. This would manifest as an error in the ram component, meaning the mostly southward flow of ∼850 m s^{-1} as seen in the frame of the northward moving payload. Assuming an average ion mass of 30 a.m.u., a 230 m s^{-1} error would result from a potential change of just 60 mV.

[29] Given the sensitivity of v_{iN} to spacecraft potential and the absence of any way to correct for such areas, it is somewhat surprising that the observed discrepancies between v_i and $\vec{E} \times \vec{B}$ and $\vec{U}$ are as small as they are. Spacecraft potential changes can result from variations in plasma density or electron precipitation environment. However, inspection of Fort Yukon all-sky camera images under the rocket trajectory and Langmuir probe-derived plasma density show no notable changes at the time of the northward ion velocity excursion in question.
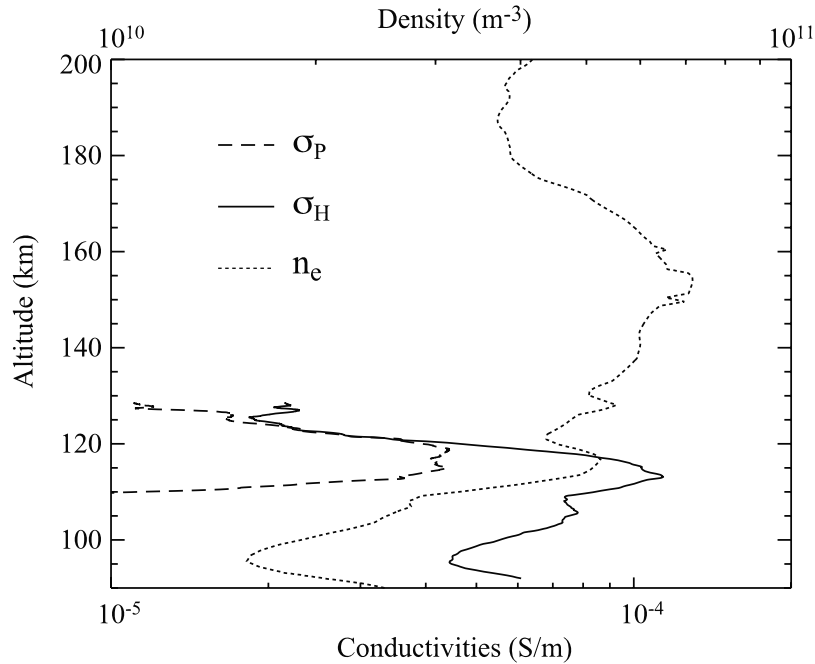
Figure 10. Pedersen and Hall conductivity profiles calculated from equations (8–10), with electron density (dotted line) overlaid.

[30] It is known that while ion velocity responds to electric field changes with a few ion cyclotron periods, the neutral wind in this altitude range requires tens of minutes [*Walterscheid et al.*, 1985]. In the 105–120 km altitude range the discrepancy between the ion velocity and the neutral wind is larger in the eastward direction than in the northward direction. This may suggest a recent change in the eastward ion flow to which the neutral wind did not have time to adapt.

4.2. New Aspects of This Study

[31] As noted in the Introduction, this is the second in situ study of ion demagnetization in the collisional transition region. The first, by *Watanabe et al.* [1991], used a single-look-direction electrostatic analyzer for the ion drift measurements and accumulated data for each ion vector over one spin. Now for the first time, a complete set of measurements of the motions of all of the coexisting gases(electrons, ions, and neutrals) have been measured with high accuracy and temporal resolution along a nearly vertical rocket trajectory through the high-latitude lower ionosphere.

[32] At 125 ion images per second, the JOULE-II SII produced velocity measurements at a much higher rate. However, careful inspection of high-passed filtered ion velocity showed no significant ion velocity fluctuations above 2 Hz. For this reason all measurements presented in this paper have been smoothed with a boxcar average at the spin frequency. We nonetheless note that the high frame rate is justified in more active environments such as substorm breakup where ion velocity and Joule heating are likely to be structured at scales of hundreds or even tens of meters as evidenced by the high degree of structure seen in breakup arcs.

[33] In addition to providing another sample to the very small set of in situ measurements of E region ion collisions,

the new contribution of this study is the inclusion of neutral wind. We have found that without neutral wind measurements, calculations of height-integrated Joule heating and conductivities would have been in error by ten or tens of percent.

[34] The conclusions of this study are as follows:

[35] 1. Ion drift velocity measured in the nightside auroral ionosphere in the altitude range 150–198 km is consistent with $\vec{E} \times \vec{B}$ motion to within 16 m s^{-1} rms.

[36] 2. Ion drift velocity measured in the altitude range 92–105 km follows the neutral wind velocity to within 20 m s^{-1} rms. This rather good agreement indicates that neutral winds are steady during the 1 min separating 21.138 UE and the TMA rocket.

[37] 3. The ion collision frequency is equal to the ion cyclotron frequency ($\kappa = 1$) at an altitude of 118 ± 0.3 km. This is consistent with the quiet time case studied by *Watanabe et al.* [1991] (although that study did not include independent measurements of the neutral wind) and with results from *St.-Maurice et al.* [1999] based on EISCAT radar measurements.

[38] 4. During this moderately active event, the height-integrated Joule heating rate was.38 W/km^2, with height-integrated Pedersen and Hall conductivities of 0.58 S and 1.13 S.

Table 1. Calculated Height-Integrated Pedersen and Hall Conductivities and Joule Heating Rate With and Without Neutral Wind Information[a]

	Units	Neglecting $\vec{U}$	Including $\vec{U}$
Σ_P	(S)	0.70	0.52
Σ_H	(S)	1.03	1.13
$\int \vec{J} \times \vec{E} \, dz$	(kW/km^2)	0.50	0.38

[a]The altitude range for the height integrations is 110–128.5 km.

[39] 5. The importance of neutral wind measurements is quantified by calculating errors that would have resulted had they not been available. Specifically, the $\kappa = 1$ altitude would have been in error by -1.5 km, the height-integrated Joule heating rate would have been overestimated by 28%, and height-integrated conductivities would have been error by $+14\%$ and -6%, respectively. Presumably, much larger errors could result in more active conditions.

[40] 6. Ion velocity during this relatively quiet period exhibited no significant variation at frequencies between 2 Hz and 62.5 Hz, corresponding to horizontal spatial scales from $\sim$350 m down to 5.5 m.

References

Burchill, J. K. (2003), GEODESIC observations of auroral ions, Ph.D. thesis, Univ. of Calgary, Alberta, Canada.

Carlson, C. W., D. W. Curtis, G. Paschmann, and W. Michel (1982), An instrument for rapidly measuring plasma distribution functions with high resolution, *Adv. Space Res.*, 2(7), 67.

Egeland, A., Ø. Holter and A. Omholt (1973), *Cosmical Geophysics*, Universitetforlaget, Oslo.

Flå, T., S. Kirkwood, and K. Schlegel (1985), Collision frequency measurement in the high-latitude E region with EISCAT, *Radio Sci.*, 20, 785.

Hanson, W. B., S. Sanatani, D. Zuccaro, and T. W. Flowerday (1970), Plasma measurements with the retarding potential analyzer on Ogo 6, *J. Geophys. Res.*, 75, 5483.

Heelis, R. A., W. B. Hanson, C. R. Lippincott, D. R. Zuccaro, L. L. Harmon, B. J. Holt, J. E. Doherty, and R. A. Power (1981), The ion drift meter for Dynamics Explorer-B, *Space Sci. Instrum.*, 5, 511.

Huuskonen, A., T. Nygren, L. Jalonen, T. Turunen, and J. Silen (1986), High resolution EISCAT observations of the ion-neutral collision frequency in the lower E-region, *J. Atmos. Terr. Phys.*, 48, 827.

Knudsen, D. J., J. K. Burchill, K. Berg, T. Cameron, G. A. Enno, C. G. Marcellus, E. P. King, I. Wevers, and R. A. King (2003), A low-energy charged particle distribution imager with a compact sensor for space applications, *Rev. Sci. Instrum.*, 74, 202.

Lathuillere, C., W. Kofman, and V. B. Wickwar (1983), Incoherent scatter measurements of ion-neutral collision frequencies and temperatures in the lower thermosphere of the auroral region, *J. Geophys. Res.*, 88, 10,137.

Nygren, T., L. Jalonen, and A. Huuskonen (1987), A new method of measuring the ion-neutral collision frequency using incoherent scatter radar, *Planet. Space Sci.*, 35, 337.

Pfaff, R. F. (1996), In-situ measurement techniques for ionospheric research, in *Modern Ionospheric Science*, edited by H. Khol et al., pp. 459–511, Eur. Geophys. Soc., Katlenburg-Lindau, Germany.

Pfaff, R. F., J. Sahr, J. F. Providakes, W. E. Swartz, D. T. Farley, P. M. Kintner, I. Haggstrom, A. Hedberg, H. Opgenoorth, and G. Holmgren (1992), The E region rocket/radar instability study (ERRRIS): Scientific objectives and campaign overview, *J. Atmos. Terr. Phys.*, 54, 779.

St.-Maurice, J.-P., C. Cussenot, and W. Kofman (1999), On the usefulness of E region electron temperatures and lower F region ion temperatures for the extraction of thermospheric parameters: A case study, *Ann. Geophys.*, 17, 1182.

Vasyliūnas, V. M., and P. Song (2005), Meaning of ionospheric Joule heating, *J. Geophys. Res.*, 110, A02301, doi:10.1029/2004JA010615.

Walterscheid, R. L., L. R. Lyons, and K. E. Taylor (1985), The perturbed neutral circulation in the vicinity of a symmetric stable auroral arc, *J. Geophys. Res.*, 90, 12,235.

Watanabe, S., B. A. Whalen, D. D. Wallis, and R. F. Pfaff (1991), Observations of ion-neutral collisional effects in the auroral E region, *J. Geophys. Res.*, 96, 9761.

Whalen, B. A., et al. (1994), The FREJA F3C cold plasma analyser, *Space Sci. Rev.*, 70, 541.

————————

D. Knudsen and L. Sangalli, Department of Physics and Astronomy, University of Calgary, 2500 University Drive NW, Calgary, AB, T2N1N4, Canada. (knudsen@phys.ucalgary.ca; sangalli@phys.ucalgary.ca)

M. Larsen, Department of Physics and Astronomy, Clemson University, Clemson, SC 29634, USA. (mlarsen@clemson.edu)

R. Pfaff, NASA Goddard Space Flight Center, Mail Code 612.3, Greenbelt, MD 20771, USA. (Robert.F.Pfaff@nasa.gov)

D. Rowland, NASA Goddard Space Flight Center, Mail Code 674, Greenbelt, MD 20771, USA. (Douglas.E.Rowland@nasa.gov)

T. Zhan, Conseco Inc., 11825 N. Pennsylvania Street, Carmel, IN 46032, USA.